Available online at www.sciencedirect.com
SCIENCE DIRECT®
International Journal of Heat and Mass Transfer 47 (2004) 5189–5200
International Journal of HEAT and MASS TRANSFER
www.elsevier.com/locate/ijhmt

Three-dimensional simulation of plasma spray: effects of carrier gas flow and particle injection on plasma jet and entrained particle behavior

Hong-Bing Xiong [a,*], Li-Li Zheng [a], Sanjay Sampath [b], Richard L. Williamson [c], Jim R. Fincke [c]

[a] Department of Mechanical Engineering, State University of New York at Stony Brook, Stony Brook, NY 11794, USA
[b] Department of Materials Science and Engineering, State University of New York at Stony Brook, Stony Brook, NY 11794, USA
[c] Idaho National Engineering and Environment Laboratory (INEEL), Idaho Falls, ID 83415, USA

Received 21 November 2003; received in revised form 2 July 2004

Abstract

As important phenomena in plasma spray, the plasma jet perturbation by the carrier gas flow and particles loading, and their effects on particle behavior are investigated. A three-dimensional computational model was developed to describe the plasma jet coupled with the orthogonal injection of carrier gas and particles. This model considered in-flight particle physical phenomena such as accelerating, heating, melting, and evaporation. The effects of carrier gas flow rates on the characteristics of plasma jet and particle spray pattern are simulated. The simulation results compare well with experimental data, for two common particle materials, NiCrAlY and ZrO_2.

Keywords: Three-dimensional simulation; Plasma spray; Jet; Carrier gas flow; Particle injection

1. Introduction

Plasma spray processes have been widely used to produce various functional metallic and ceramic coatings for wear-, corrosion-, erosion-resistance and thermal protection, due to its relative high flame temperature. To manufacture a good quality coating with desirable functionality, the control and optimization of this process still need to be improved based on the scientific understanding of the complex heat, momentum and mass transport phenomena involved. The modeling of plasma spray process has received considerable attention during the last few decades [1–8], as well as the interaction between the in-flight particles and the plasma jet [9–12]. Most of these efforts were primarily conducted in 2D configurations. The effects of carrier gas flow and particle injection are typically neglected in these models because the complex 3D interaction of carrier gas with the jet cannot be accurately modeled with an axisymmetric assumption. However, the carrier gas flow injection, which enables the particle entrainment in the high-temperature high-velocity plasma jet, does disturb the flame and has significant influence on the in-flight particle

* Corresponding author. Tel.: +1 631 632 1490; fax: +1 631 632 8544.
E-mail address: hxiong@ic.sunysb.edu (H.-B. Xiong).

0017-9310/$ - see front matter © 2004 Elsevier Ltd. All rights reserved.
doi:10.1016/j.ijheatmasstransfer.2004.07.005

Nomenclature

C_p	specific heat, $J\,kg^{-1}\,K^{-1}$	$\mathbf{U},\mathbf{V}$	velocity vector, $m\,s^{-1}$
C_D	drag coefficient	$\mathbf{V}'$	velocity fluctuation, $m\,s^{-1}$
h	convective heat transfer coefficient, $W\,m^{-2}\,K^{-1}$	y	axial coordinate, m
k	thermal conductivity, $W\,m^{-1}\,K^{-1}$	*Greek symbols*	
L_m	latent heat of fusion, $J\,kg^{-1}$	ε	emissivity
L_{evap}	latent heat of evaporation, $J\,kg^{-1}$	μ	viscosity, $kg\,s^{-1}\,m^{-1}$
Pr	Prandtl number	θ	circular coordinate
r, R	radial coordinate, m	ρ	density, $kg\,m^{-3}$
Re_p	Reynolds number of particle, $\rho_f D_p \mid \widetilde{V} + V' - V_p \mid /\mu_f$	*Subscripts*	
Sh	Sherwood number	p	particle
t	time, s	l	liquid
T	temperature, K	s	solid

characteristics [13,14]. The understanding of carrier gas effects on plasma jet and particle behavior is desirable for the control and design of plasma spray process.

The study of three-dimensional behavior of the plasma jet reflecting actual conditions has been started in the last few years [3–8]. Ahmed and Bergman [4] studied the ceramic particles in Ar–H_2 plasma jet using a 3D model coupled with the commercial computational code FLUENT. Li and Chen [5] developed a three-dimensional computational model that is capable of handling transverse carrier gas injection and its influence on the plasma jet behavior and particles trajectories. Mariuax et al. [8] and Vardelle et al. [7] have performed 3D simulations for the plasma spray process, in which the conversion of energy in the torch nozzle, from electric power to thermal energy, is considered. However, most authors use empirical velocity and temperature profiles at the nozzle exit matching with the plasma gas mass flow rate and its enthalpy, due to the complexity of the arc dynamics inside the torch with its attachment to the anode-nozzle wall [15]. The local thermodynamic equilibrium is also generally assumed. Noted that most three-dimensional models so far are based on the assumption that the particle is in uniform temperature during in-flight. And some models neglect the effects of particles on the plasma gas.

In this study, a three-dimensional transient model for plasma jet and particle is developed to investigate the plasma jet perturbation by carrier gas and particle loading, and their effects on the in-flight particle behavior. The plasma jet and the particle trajectory are described in the three-dimensional geometry, and the non-thermal equilibrium of the particle in-flight is considered by employing one-dimensional thermal model. This model is incorporated into the LAVA code, originally developed at INEEL in a two-dimensional geometry. The modified computational code LAVA-P-3D is tested with experiment and further applied to thermal spray process. The numerical simulations are performed to investigate the three-dimensional behavior of the plasma jet and its influence on particle in-flight velocity and temperature.

2. Plasma jet modeling

The schematic presentation of plasma spray process and computational geometry is displayed in Fig. 1a. The plasma jet is treated as a compressible, multi-component, turbulent, reacting flow with temperature-dependent thermodynamic and transport properties with the assumption of local thermodynamic equilibrium. The plasma jet is described in the three-dimensional cylindrical geometry, with spatial coordinate (r, y, θ) indexing radial, axial and circular directions, respectively. The continuity equation for species i, and the mass, momentum and energy conservation equations for the fluid mixture are written in terms of vectors and tensors as follows [2]:

$$\frac{\partial \rho_i}{\partial t} + \nabla \cdot (\rho_i \vec{u}) = -\nabla \cdot \vec{J}_i + \dot{\rho}_i^c, \tag{1}$$

$$\frac{\partial \rho}{\partial t} + \nabla \cdot (\rho \vec{u}) = 0, \tag{2}$$

$$\frac{\partial (\rho \vec{u})}{\partial t} + \nabla \cdot (\rho \vec{u}\vec{u}) = -\nabla \left(p + \frac{2}{3}\rho k \right) + \nabla \cdot [\sigma] + F_p, \tag{3}$$

$$\frac{\partial (\rho e)}{\partial t} + \nabla \cdot (\rho e \vec{u}) = -p \nabla \cdot \vec{u} - \nabla \cdot \vec{q} + \rho \varepsilon + \dot{Q}_c - \dot{Q}_R + \dot{Q}_p, \tag{4}$$

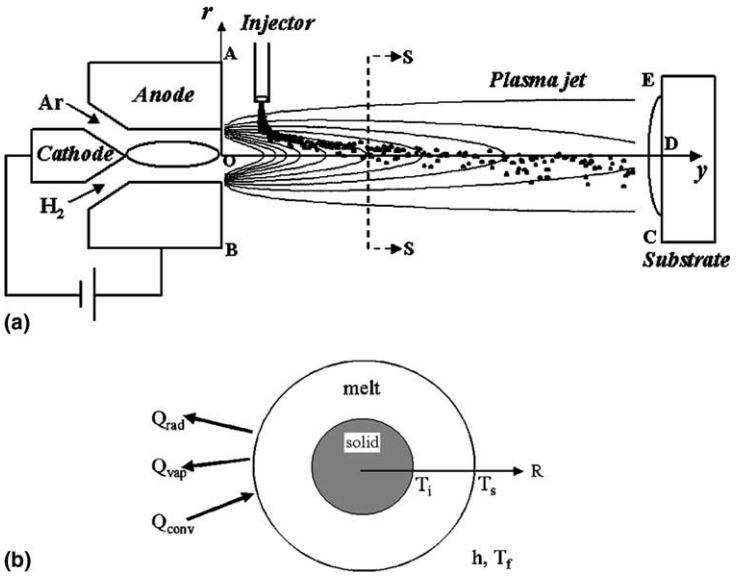

Fig. 1. Schematic diagram of (a) plasma spraying process using a DC plasma torch and (b) the particle heat transfer.

where ∇ is the vector differential operator in cylindrical coordinate. In Eq. (1), J_i is the diffusion mass flux and $\dot{\rho}_i^c$ is the rate of density change due to chemical reaction. F_p in Eq. (3) represents the momentum source or sink due to particles injection, k is the turbulent kinetic energy per unit mass, σ is the viscous shear stress tensor given by

$$[\sigma] = (\mu + \mu_t)\left[\nabla\vec{u} + (\nabla\vec{u})^T\right] + (\lambda + \lambda_t)\nabla\cdot\vec{u}\, I, \tag{5}$$

where μ is the molecular viscosity, μ_t is the turbulent viscosity, $\lambda = -2\mu/3$, $\lambda_t = -2\mu_t/3$, and I is the unit matrix. The standard k–ε model is used to calculate the effective turbulence effects. In Eq. (4), $\vec{q}$ is the heat flux vector, ε is the viscous dissipation rate, $\dot{Q}_c$ is the rate of internal energy change due to chemical reactions, $\dot{Q}_R$ is the heat loss rate due to radiation, and $\dot{Q}_p$ is the heat source or sink due to injected particles. The plasma is assumed optically thin; therefore the radiative heat loss can be treated as temperature-dependent volumetric sink term. The thermodynamic and transport properties of the gas mixture are calculated from the ideal gas state relations using the temperature-dependent properties for each species from Ref. [16]. The ionization, dissociation, recombination, and other chemical reactions are treated using a general kinetic and equilibrium reaction algorithm [1]. A reduced set of reactions consisting of chemical species Ar, Ar^+, H_2, H, H^+, N_2, N_2^+, N, N^+, O_2, O, O^+, and e^-, is used for the argon–hydrogen plasma. Detailed descriptions of the governing equations and numerical solutions can be found in previous literatures [1,2].

3. Particle modeling

The injected particles are discretely treated in a Lagrangian manner. Computational particles are generated at the points of injection and tracked throughout their flight. The solution of the plasma gas provides the information on conditions external to the particle. A one-dimensional model of particle heating and melting is used in which a spherical shape of the particle, as shown in Fig. 1b, is assumed. The internal convection within the molten part of the particle is neglected.

Momentum transport. Driving forces on a particle immersed into a plasma jet include the viscous drag, the pressure gradient and gravitational force. The drag force is assumed as the only prominent one that affects the particle momentum transfer significantly for the particle size smaller than 100 μm [10]. The momentum transfer between the particle and plasma jet can be described by:

$$\frac{d\vec{V}_p}{dt} = \frac{3}{8}\frac{\bar{\rho}}{\rho_p}\frac{C_D}{r_p}\left|\tilde{\vec{V}} + \vec{V}' - \vec{V}_p\right|\left(\tilde{\vec{V}} + \vec{V}' - \vec{V}_p\right), \tag{6}$$

where $\vec{V}'$ is the velocity fluctuation, approximating the fluctuating effect of turbulence on tiny particles. The coefficient C_D for the drag force is expressed as:

$$C_D = \left(\frac{24}{Re_p} + \frac{6}{1+\sqrt{Re_p}} + 0.4\right) f_{prop}^{-0.45} f_{Kn}^{0.45} \quad \text{for } Re_p < 100, \tag{7}$$

where f_{prop} and f_{Kn} account for the effects of variable plasma properties and Knudsen non-continuum, respectively [9–11].

Energy and mass transport. The temperature distribution inside the particle is described by conduction as follows:

$$\rho_p C_p \frac{\partial T}{\partial t} = \frac{1}{r^2}\frac{\partial}{\partial r}\left(k_p r^2 \frac{\partial T}{\partial r}\right). \tag{8}$$

The boundary conditions at the particle center and surface are given as:

$$\left.\frac{\partial T}{\partial r}\right|_{r=0} = 0 \quad \text{and}$$
$$4\pi r_p^2 \left(k_p \frac{\partial T}{\partial r}\right)\Big|_{r=r_p} = \dot{Q}_{conv} - \dot{Q}_{vap} - \dot{Q}_{rad}. \tag{9}$$

The heat flux at the particle surface by convection, radiation and evaporation, $\dot{Q}_{conv}$, $\dot{Q}_{rad}$ and $\dot{Q}_{vap}$, are expressed as $4\pi r_p^2 h\left(\widetilde{T}_f - T_s\right)$, $4\pi r_p^2 \varepsilon\sigma\left(T_s^4 - \widetilde{T}_\infty^4\right)$ and $\dot{m}_v L_v$ respectively [11]. The convective heat transfer coefficient, h, is calculated from the Nusselt number:

$$Nu = \frac{2hr_p}{k_f} = \left(2.0 + 0.6 Re_p^{1/2} Pr^{1/3}\right)(f_{prop})^{0.6} f_{Kn} f_v, \tag{10}$$

where f_v accounts for the effect of mass transfer due to evaporation [12]:

$$f_v = \frac{\dot{m}_v c_{p,f}/2\pi r_p k_f}{\exp\{\dot{m}_v c_{p,f}/2\pi r_p k_f\} - 1}, \tag{11}$$

f_v approaches one when the evaporation mass rate $\dot{m}_v$ is close to zero. f_v is smaller than one when $\dot{m}_v$ is larger than zero. This indicates that the convective heat flux becomes smaller when accounting for the evaporation. A more comprehensive study has been reported by Chen [17] to establish the correlation between the heat and mass transfer under thermal plasma environment. In the calculation of radiation heat flux, only the radiation between the particle surface and the environment is considered in the case of optically thin plasma gas. The evaporation mass rate, $\dot{m}_v$, is either controlled by the vapor diffusion through the boundary layer around the particle, or the heat transfer through the particle [12]:

$$\dot{m}_v = \min\left\{2(\bar{\rho} D_g)_f \pi r_p \ln(1+B) Sh, \dot{Q}_{net}/L_v\right\}, \tag{12}$$

where Sh, the Sherwood number, accounts for convective mass transfer; and B, the mass transfer number, related to the local mass fraction of vapor in the gas phase and the vapor concentration on the droplet surface. If a particle is subjected to melting or re-solidification, the additional constraints will be applied to the melting or re-solidification interfaces:

$$\left(k_p \frac{\partial T}{\partial r}\right)\Big|_{r=r_m^-} - \left(k_p \frac{\partial T}{\partial r}\right)\Big|_{r=r_m^+} = L_m \rho_p \frac{dr_m}{dt}$$
$$\text{or} \quad \left(k_p \frac{\partial T}{\partial r}\right)\Big|_{r=r_s^+} - \left(k_p \frac{\partial T}{\partial r}\right)\Big|_{r=r_s^-} = L_m \rho_p \frac{dr_s}{dt}. \tag{13}$$

The actual interface temperature, T_i, is related to the interface movement by [18]:

$$\frac{dr_m}{dt} = \mu_k (T_m - T_i), \tag{14}$$

by considering a non-equilibrium melting and solidification. μ_k is the linear kinetic coefficient. The values of μ_k for Zirconium and NiCrAlY are 0.01 and $0.85\,m\,s^{-1}K^{-1}$. Heat transfer and phase change within the particle and mass transfer from its surface can then be calculated based on this model.

4. Computational issues and boundary conditions

To accurately predict the 3D plasma jet and in-particle behavior, special treatments have been proposed and incorporated into a jointing developed code LAVA-3D-P, for the computational domain, boundary conditions, the side injector, carrier gas injection, and multiple particle injection.

4.1. Basic description of the problem

The present study is conducted for a DC plasma system that uses Metco 9MB plasma gun with the inner, R_i, and outer, R_o, radius of the nozzle as 0.39 cm and 1.5 cm, respectively. The powder materials of NiCrAlY and zirconia (ZrO_2) subjected to heating by the argon–hydrogen plasma jet have been simulated for the initial particle size ranging from 5 to 120 μm. The injector is located at 8 mm above the plasma central axis, and 6 mm from the plasma gun exit. As listed in Table 1, two cases of the operating conditions are simulated using the three-dimensional numerical program. The particles conditions of NiCrAlY and ZrO_2 and their properties are listed in Table 2.

4.2. Geometry and boundary conditions

The computational domain and some of the boundary conditions employed in the calculation of plasma jet are described in Fig. 2. The simulation is based on the three-dimensional computational domain, with the mesh size of $28 \times 48 \times 32$ in the cylindrical coordinate (r, y, θ) system. The radius and axial lengths of the com-

Table 1
Operating conditions for plasma jet and carrier gas flow

Processing parameters	Case 1	Case 2
First plasma gas, Ar, SLM[a]	40	40
Secondary plasma gas, H_2, SLM	7	12
Arc current, A	500	600
Voltage, V	61	75
Carrier gas flow rate, Ar, SLM	1.5–15.0	4.0–7.0

[a] SLM means standard liter per minute; 1 slm = $16.67\,cm^3\,s^{-1}$.

Table 2
Particle conditions

Particle material	ZrO_2	NiCrAlY
Feeding rate, $kg\,h^{-1}$	1.2	2.0
Average size, μm	30	50
Stand distance, mm	100	100
k_s, $W\,m^{-1}\,K^{-1}$	2.0	74
k_l, $W\,m^{-1}\,K^{-1}$	3.0	43
$C_{p,s}$, $J\,kg^{-1}\,K^{-1}$	580	448
$C_{p,l}$, $J\,kg^{-1}\,K^{-1}$	713	448
ρ_s, $g\,cm^{-3}$	5.89	8.1
ρ_l, $g\,cm^{-3}$	5.89	8.1
T_m, K	2950	1411
L_m, $kJ\,kg^{-1}$	812.4	299
L_v, $kJ\,kg^{-1}$	6000	7330

putational regime are 6 cm and 15 cm, respectively; while 2π in the circular direction. The calculations are initialized from the cold air mixing with the incoming jet until the steady state is reached.

At the nozzle exit ($y = 0$), the temperature and axial velocity of the plasma jet are estimated from [1]:

$$v(r) = V_{cl}[1 - (r/R_i)^m] \quad \text{and}$$
$$T(r) = (T_{cl} - T_w)[1 - (r/R_i)^n] + T_w, \tag{15}$$

where V_{cl} and T_{cl} are the maximum values of plasma velocity and temperature, whereas T_w is the wall temperature. For example, we select $V_{cl} = 2560.3\,m\,s^{-1}$, $m = 1.2$, $T_{cl} = 12987.7\,K$ and $n = 6$ for case 1 to match the known flow rate and the power supplied to the plasma gun in the experiments [19]. The turbulence wall function treatment is employed in the torch wall, and both open boundaries and the downstream boundary are taken as either inward or outward flow conditions [1]. The periodic boundary condition is used at the circular direction as $\phi\,(r, y, 2\pi) = \phi(r, y, 0)$. At the axis of the jet, the symmetrical condition can be applied for 2D simulation by neglecting the effects of carrier gas and entrained particles; however this assumption is not applicable for three-dimensional simulation. To include

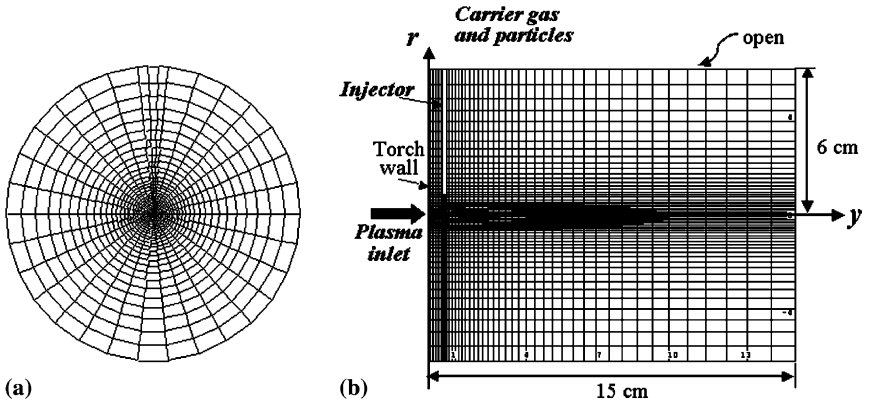

Fig. 2. Geometry, computational mesh and boundary conditions in: (a) cross-section plane in radial and azimuthal directions, (b) middle section plane of 3D plasma jet.

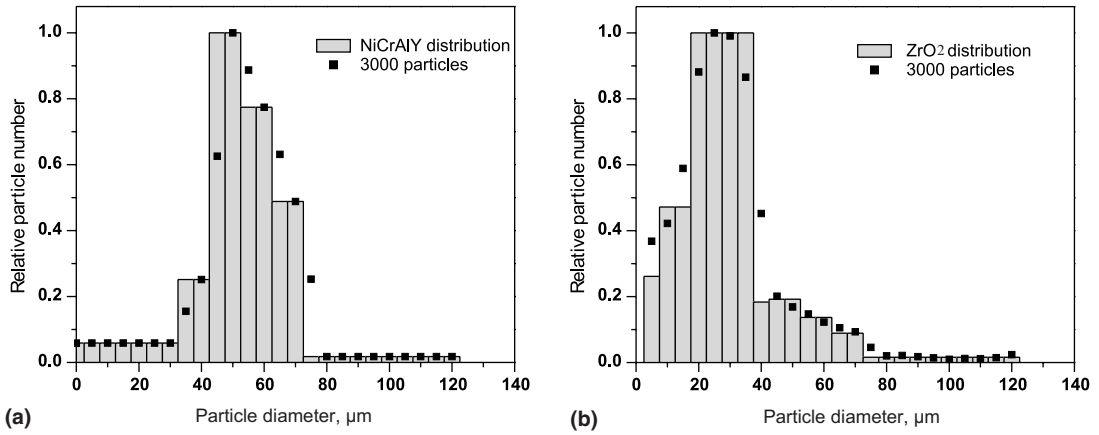

Fig. 3. (a) NiCrAlY, and (b) ZrO2 particle size distribution from sieving and the data achieved in the simulation.

the non-asymmetric effects, the boundary at the axis is specified in 3D simulation as follows:

$$\phi|_{r=0} = \left(\sum_{i=1}^{N}\phi_i\right) \Big/ N(\phi = u, v, T) \quad \text{and} \quad w = 0, \quad (16)$$

where ϕ_i are the values of ϕ at locations with the distance Δr from the centerline.

4.3. Side injector and carrier gas

The side injector is treated as a solid block that has zero diffusivity and infinitely large viscosity. The thermal conductivity of this solid block is assumed as $80\,\mathrm{W\,m^{-1}\,K^{-1}}$. The meshes for the side jet nozzle exit have been refined with a grid size of 6×3 for the nozzle diameter of 1.8 mm (see Fig. 2). The carrier gas is treated as an additional source adding to the momentum and energy at the control volumes that contain the side injector nozzle exit plane. Injected particles are also treated as momentum and energy source terms for the control volumes where the particles reside.

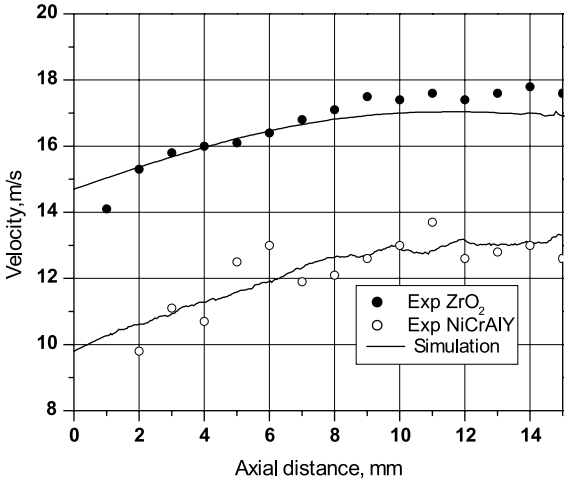

Fig. 4. Particle velocity along the centerline of the side injector after particles exit from the injector, where the solid line represents the simulation result, and symbols are experimental results.

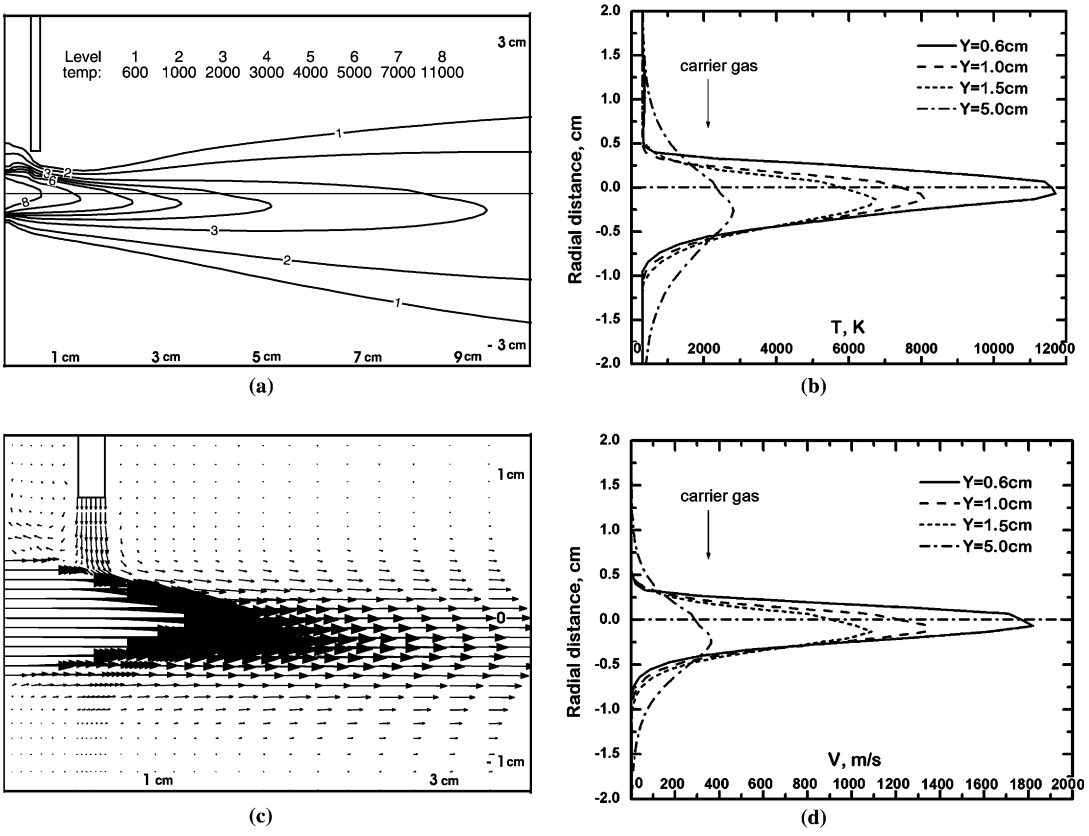

Fig. 5. Gas temperature: (a) contours at the ABCE plane (indicated in Fig. 1) and (b) gas temperature profiles at the cross lines of the ABCE plane. Gas velocity: (c) vector at the ABCE plane (indicated in Fig. 1) and (d) gas axial velocity profiles at the cross lines of the ABCE plane (lines parallel to AB or CE in Fig. 1), for carrier gas flow rate of 15 slm.

4.4. Particle injection

The entrained particles are discretely treated in a Lagrangian coordinate and stochastically generated by sampling from the probability distributions of the particle size and its velocity at the injection nozzle. Multiple particles have size, velocity, direction and position distributions at injection. Fig. 3 shows the particle size distributions in the simulations along with the original sampling of particle size distribution achieved from experiments, for NiCrAlY and ZrO_2 respectively. The velocity assigned to each particle is the measured average particle velocity at the injector exit with a random deviation within 5%; the direction with regard to injector axis is given by a random distribution from 0 to 20°. The particle positions are randomly distributed in the exit plane of the injector. About 2000–3000 particles are injected in the flow after introducing the carrier gas.

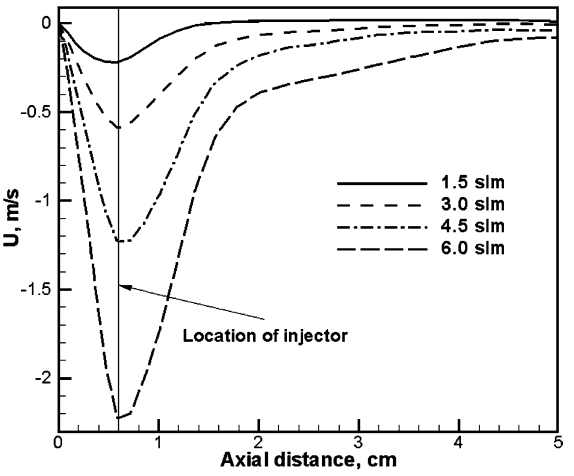

Fig. 6. Gas radial velocity at the centerline of the plasma jet with different carrier gas flow rates.

5. Experiment and validation of LAVA-P-3D

5.1. Experiment at INEEL

The numerical results have been compared with the experiments conducted at INEEL [13]. Their experiment used a Metco 9MB spray gun and Miller model 1270 powder feeders, with spray conditions as case 2 listed in Table 1. The powders, Praxair NiCrAlY, Ni-346-1 and Sulzer-Metco stabilized zirconia, 204NS, were roughly spherical as supplied. The particle size distributions were obtained by sieving experimentally, as shown in Fig. 3; such data were used for the multiple particle generation in the simulation.

In the experiment, the Torch Diagnostic System (TDS-1610) and the Inflight Particle Pyrometer (IPP-2000) were used to measure the particle trajectory information and ensemble particle temperature. Particle velocity and size were measured by the Aerometrics Phase Doppler Particle Analyzer (PDPA) system. The averaged particle injection velocity and carrier gas velocity have been measured at the 2mm downstream of the injector tip for different carrier gas flow rate; the results are used as input data for the simulation.

5.2. Validation of LAVA-P-3D

The LAVA 3D code has been validated through the original well-tested LAVA 2D code; both the LAVA 3D and the particle injection in three-dimensional plasma jet have been proved to work correctly [20]. In order to further validate this newly developed LAVA-P-3D program, the numerical results have also been compared with experimental data. Due to the lack of the experimental data for plasma gas velocity and temperature, the validation of numerical model is currently restricted

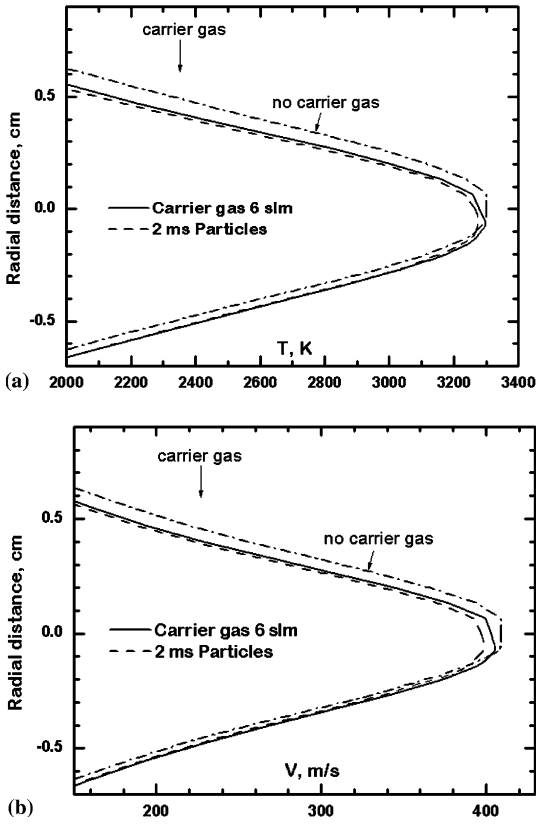

Fig. 7. (a) The axial velocity and (b) temperature at the cross line away from nozzle 5cm. The solid, dash, and dash-dot lines are for cases with carrier gas of 6 slm, and then with zirconia particle injected along with carrier gas at 1.5 $g\,s^{-1}$, and without carrier gases respectively.

to the particle velocity and temperature; in this case the particle average velocity after injection is compared with the experiment results. Both experiment and simulation were conducted based on the same operating conditions, as case 2 listed in Table 1. The predicted particle velocity at the centerline of the injector after injection is plotted against the experimental data [13] in Fig. 4 for zirconia and NiCrAlY particles. A good agreement between the simulation results and experimental data has been obtained; the difference between the experiment and simulation is within 10%.

6. Results and discussion

6.1. Effects of carrier gas flow on plasma jet

To examine the side injection effect, the 3D cases based on the operating conditions of case 1 listed in Table 1 have been simulated. The Ar carrier gas is injected from the side injector located at 8 mm above the plasma central axis, with gas flow rate varying from 1.5 to 15 slm. Fig. 5a shows the gas temperature contours in the plasma jet at the cross-section of ABCE with carrier gas rate 15 slm; Fig. 5c shows the gas velocity vector at this plane. It is clear that the temperature contour is not symmetric about the axis of the jet, rather shifts from the centerline towards the bottom, which is believed as the result of side carrier gas injection. This shift is aggravated at the downstream of the plasma jet. For the carrier gas flow rate of 1.5–6 slm, the angle between the plasma jet axis and the torch axis is about one degree, while for carrier gas flow rate of 15 slm it has the larger angle of 2.9°. The influence of carrier gas injection on plasma jet fluid can be very large, depending on the carrier gas flow rate, injection location and plasma conditions. For example, for carrier gas rate 15 slm in this case, the flow pattern of the plasma jet is

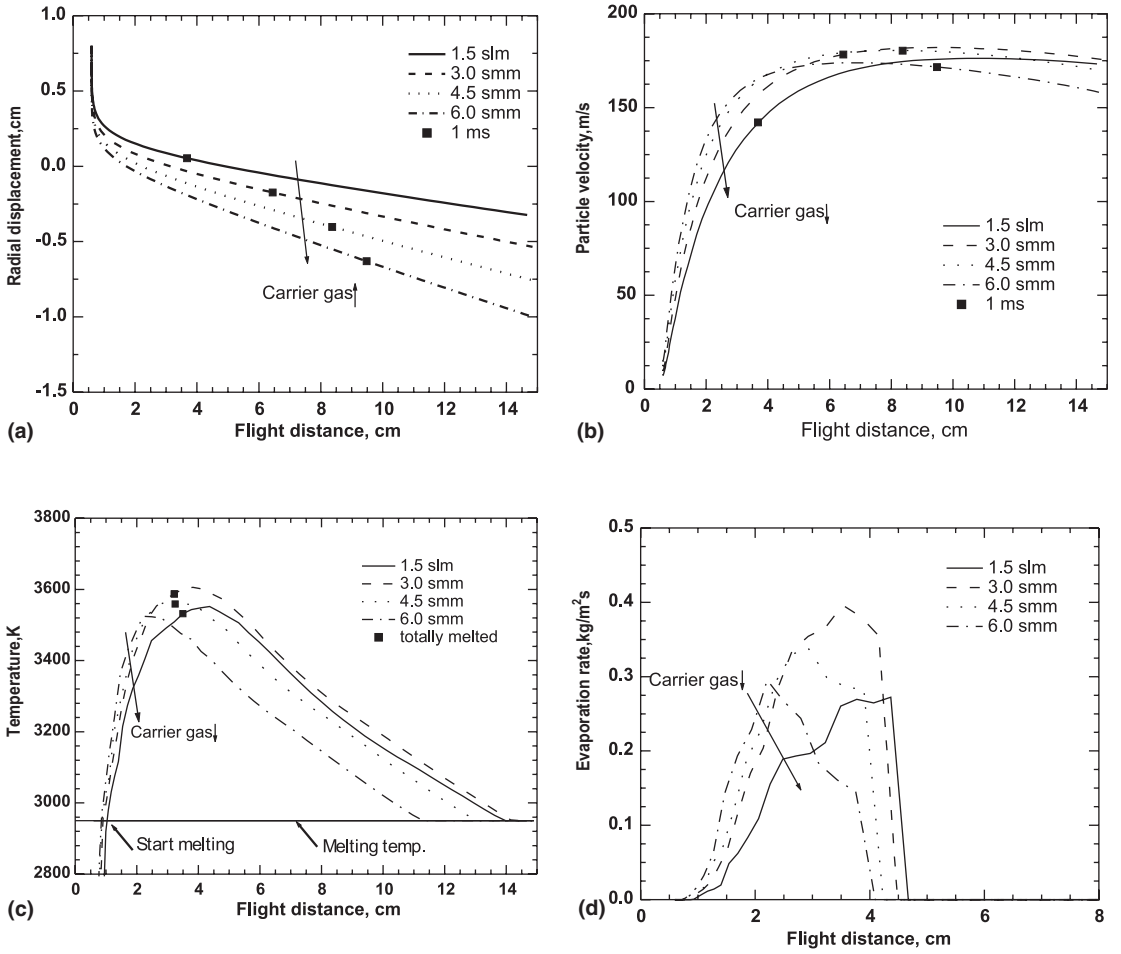

Fig. 8. Dependency of in-flight behaviors for Zirconia particles of diameter 30 mm vs. carrier gas flow rates ranging from 1.5 to 6 slm: (a) particle trajectories for ZrO_2, (b) particle velocity of ZrO_2, (c) particle temperature of ZrO_2, and (d) evaporation of ZrO_2 particle with different size.

significantly influenced by the injection of carrier gas, especially at the area downstream of the injector. The vortex induced by the carrier gas flow is also present in the area adjacent to the injector, as shown in Fig. 5c. For quantitative results, Figs. 5b and d show the temperature and axial velocity profiles at the cross lines that crosses the plasma jet axis and is parallel to line AB (see Fig. 1) for the carrier gas flow rates of 15 slm. Solid, dashed, dotted, and dash-dot lines represent the results at the downstream distance of 0.6, 1.0, 1.5 and 5 cm, respectively, where the arrows indicate the direction of the carrier gas injection; that is from top to bottom.

The effects of carrier gas flow rate on the plasma jet velocity and temperature are shown in Fig. 6, which represents the gas radial velocity at the centerline of plasma jet (line OD in Fig. 1a) with carrier gas flow rates of 1.5, 3.0, 4.5, and 6.0 slm. By increasing carrier gas flow rate, the radial velocity increases at the centerline. The injection of carrier gas results in the deflection of the plasma jet and such deflection is aggravated by the increasing carrier gas flow rate. As a result, the flow change will directly affect the particle velocity and trajectory after leaving the injector exit. The loading of multiple particles will also disturb the plasma jet flow. With the injection of multi-particles, the temperature of the plasma jet will decrease due to the energy transferred to the cold particles. Dashed lines in Fig. 7, representing the axial velocity and temperature after zirconia particle injection for 2 ms at feeding rate of 1.5 g s^{-1}, show the decrease in temperature and axial velocity of the plasma jet after particle injection, indicating the influence of multi-particles in plasma jet.

6.2. Effects of carrier gas flow rate on entrained particle behavior

The effects of carrier gas flow rates on single zirconia particle behavior are shown in Fig. 8. In the case of high carrier gas flow rate, the particle exhibits a higher transverse velocity and penetrates further down toward the plasma jet; the plasma jet is also perturbed and cooled by the carrier gas. Therefore, different particle velocity

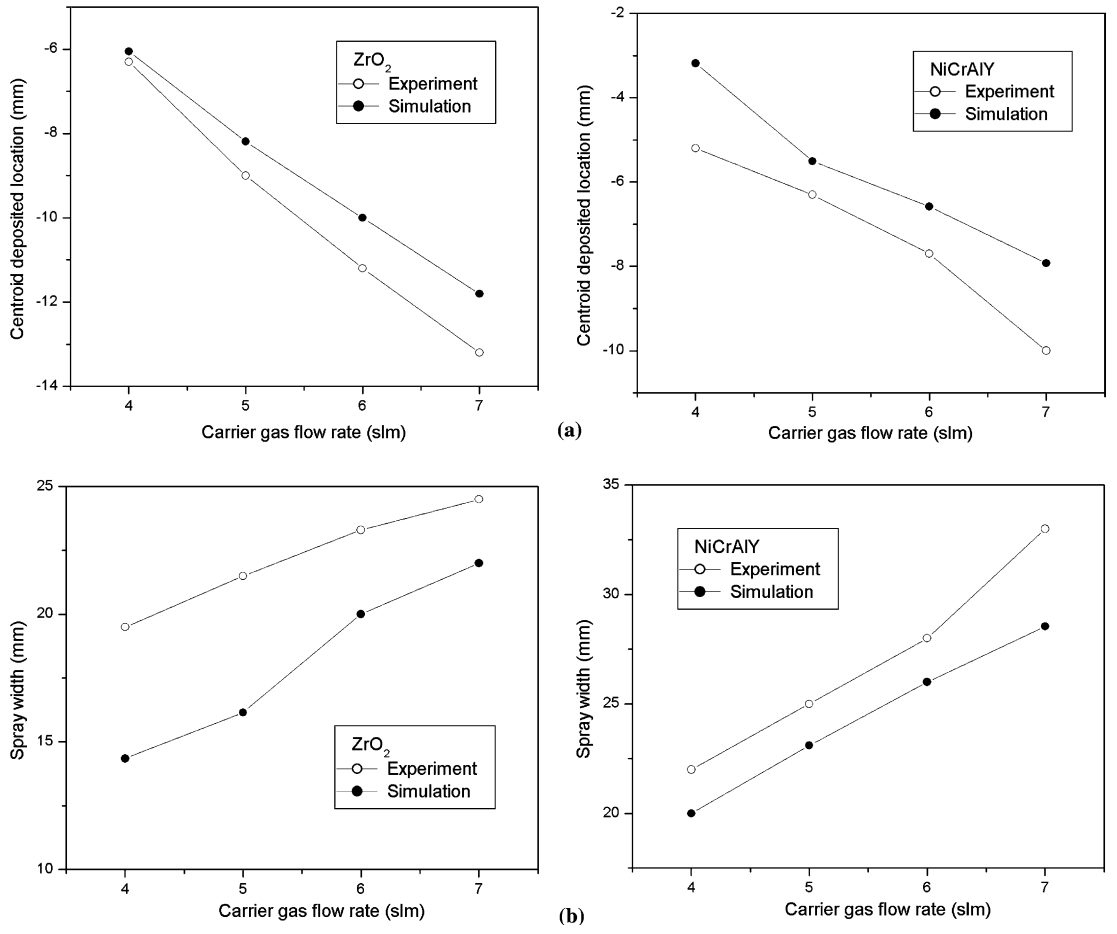

Fig. 9. (a) Spray pattern centroid position and (b) spray pattern width as a function of carrier gas flow rate.

and temperature histories are obtained for the same size of zirconia particle with the diameter 30 μm. Results show that although particle trajectory and deposition location are greatly influenced by carrier gas, the particle velocity and temperature are not sensitive to the change of carrier gas. Firstly, particles in the high carrier gas flow rate experience a steep acceleration when entrained into the hot core of the plasma jet, but it will slow down at the peripheral areas of the plasma jet. As a result, similar particle velocities are obtained at the typical spray distances from 6 to 15 cm for different carrier gas flow rates. Secondly, the particle evaporation and fusion contribute to the weak influence of carrier gas flow rate on the particle temperature. As indicated in Fig. 8, although the particle in 3 slm carrier gas is heated more rapidly and gain more energy compared to that in 1.5 slm carrier gas, the evaporation of this particle is much larger and its temperature increases not too much due to the huge latent heat of evaporation. Another case, is the particle in 6 slm carrier gas that absorbs less heat since it is overshoot and flies out the hot core of plasma jet quickly, which results partially melted but temperature is still close to the melting point at spray distance of 10 cm.

The multiple particle spray pattern has also been studied under different carrier gas flow rates, with concerns of pixel deposition position and spray width of the particles upon impact. Pixel position, or centroid position is the peak of the particle radial distribution. Spray width is defined as the width of the spatial distribution of particles with particle number intensities greater than 10% of the maximum intensity observed at the pixel position of spray pattern. The pixel position and spray width from experiment and simulation are shown in Figs. 9a and b for the case 2 with spray distance of 10 cm, for NiCrAlY and ZrO_2 respectively. For both the NiCrAlY and ZrO_2 particles, the spray pattern pixel position decreases with carrier gas increase, and the spray width monotonically increases.

The average particle velocity and temperature for different carrier gas flow rates are also investigated. Since IPP measures a large number of particles simultaneously based on their radiance, and yields an estimated mean

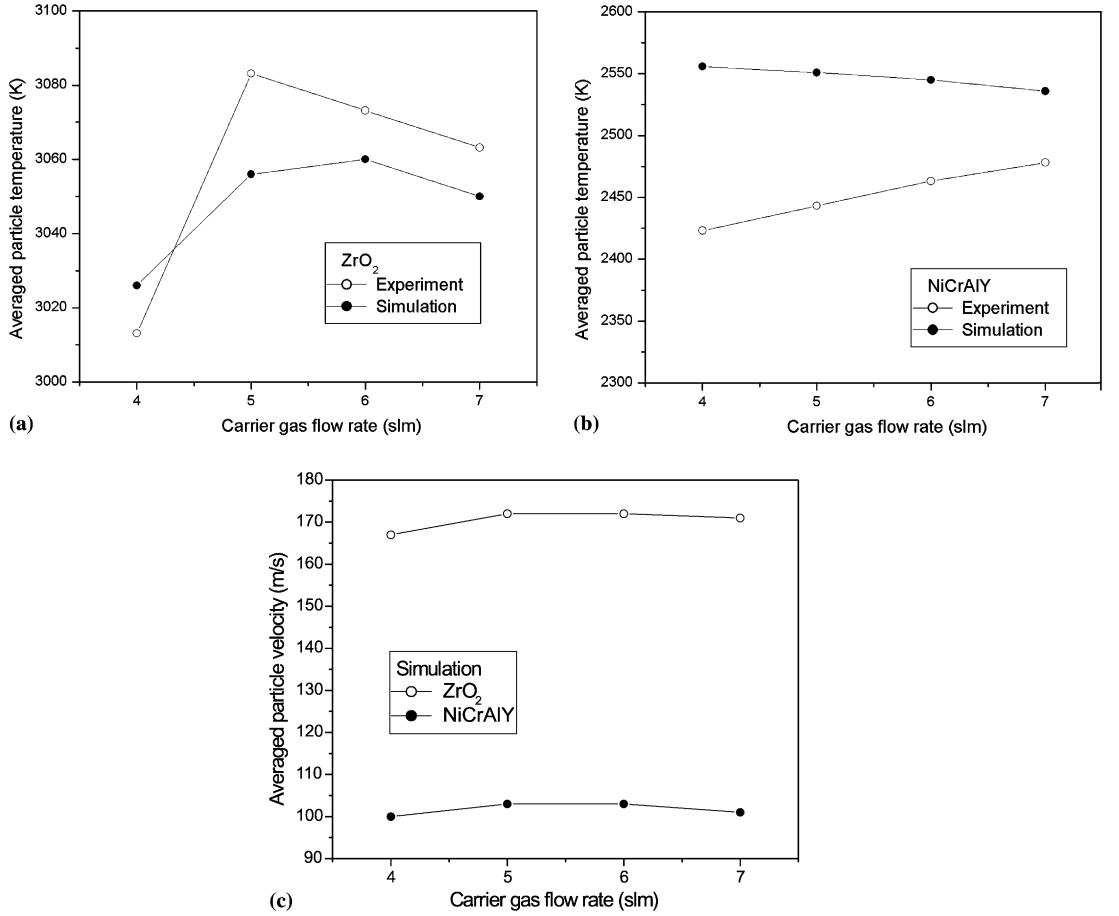

Fig. 10. Average particle temperature for (a) zirconia, (b) NiCrAlY, and (c) average particle velocity as a function of carrier gas flow rate.

particle temperature. This ensemble temperature is related to the distribution of particle size and temperature. As particle radiance is approximately proportional to particle surface area and particle temperature's fourth power, the simulated averaged particle temperature is also weighted by D_P^2 and T_P^4. The effects of carrier gas flow rates on the average particle temperature and velocity at the spray distance of 10 cm are depicted in Fig. 10a–c. Both experiment and simulation show that the particle temperature is not so sensitive to carrier gas, with difference range within 100 K, although the spray pattern is greatly changed. Simulation data also show that the average particle velocities, which are algebraic average based on all the particles collected, vary in a short range of $10\,m\,s^{-1}$ for the carrier gas flow rates ranging from 4 to 7 slm. Compared with experimental data (see Figs. 9 and 10), the simulation results fit well with the experiment, except that the spray width is less than experiment. Noted that in the simulation, we did not consider the fluctuation of arc root within the anode. In fact, the fluctuation of arc root causes the fluctuations of spray particles and thus a wider distribution of particle trajectories, velocities and temperatures upon impact. Therefore a smaller spray width from prediction is expected without considering arc fluctuation.

7. Conclusions

A three-dimensional program has been developed based on two-dimensional LAVA code by incorporating the effects of carrier gas and multiple particle injection. Using the LAVA 3D program, numerical studies have been conducted to investigate the effects of carrier gas injection on the characteristics of plasma jet. Results show the perturbation of plasma jet due to the impact of side jet, as well as the cooling and slowing effects of the plasma jet due to carrier gas and multi-particles injection. The effects of carrier gas flow rate on the entrained particles behavior have also been investigated, for the powder materials of NiCrAlY and ZrO_2. The carrier gas flow rate affects the particle trajectories and thus the particle velocity and temperature histories. It is found that the particle spray pattern is greatly influenced by the carrier gas flow rate, while particle temperature and velocity is not sensitive to it. The numerical results have been compared with experiments and a good agreement has been achieved.

Acknowledgments

This work is supported by the NSF through CTS-0074589 and DMR MRSEC-0080021, as well as the DOE through a subcontract from the INEEL.

References

[1] J.D. Ramshaw, C.H. Chang, Computational fluid dynamics modeling of multi-component thermal plasmas, Plasma Chem. Plasma Process. 12 (1992) 299–325.
[2] C.H. Chang, J.D. Ramshaw, Numerical simulation of nonequilibrium effects in an argon plasma jet, Phys. Plasmas 1 (11) (1994) 3698–3708.
[3] Z. Njah, J. Mostaghimi, M. Faghri, M. Boulos, Study of 3-D mixing of a cold jet with a transverse plasma stream, Int. J. Heat Mass Transfer 36 (16) (1993) 3897–3907.
[4] I. Ahmed, T.L. Bergman, Simulation of thermal plasma spraying of partially molten ceramics: effect of carrier gas on particle deposition and phase change phenomena, Trans. ASME 123 (2001) 188–196.
[5] H.-P. Li, X. Chen, Three-dimensional simulation of the turbulent plasma jet impinging upon a flat plate and with transverse particle and carrier gas injection, Plasma Chem. Plasma Process. 22 (2002) 27–57.
[6] K. Ramachandran, H. Nishiyama, Three-dimensional effects of carrier gas and particle injections on the thermo-fluid fields of plasma jets, J. Phys. D: Appl. Phys. 35 (2002) 307–317.
[7] M. Vardelle, A. Vardelle, P. Fauchais, K.-I. Li, B. Dussoubs, N.J. Thermelis, Controlling particle injection in plasma spraying, J. Thermal Spray Technol. 10 (2001) 267–284.
[8] G. Mariaux, E. Legros, A. Vardelle, Modeling of coating formation and heat flux to substrate by particles and plasma jet in plasma spraying, in: C. Moreau, B. Marple (Eds.), Thermal Spray 2003: Advancing the Science and Applying the Technology, ASM Int., OH, USA, 2003, pp. 895–903.
[9] Y.C. Lee, K.C. Hsu, E. Pfender, Modeling of particles injected into a D.C. plasma jet, Proc. 5th Int. Symp. Plasma Chem. 2 (1981) 795.
[10] X. Chen, E. Pfender, Behavior of small particles in a thermal plasma flow, Plasma Chem. Plasma Process. 3 (3) (1983) 351–366.
[11] Y.P. Wan, V. Prasad, G.-X. Wang, S. Sampath, J.R. Fincke, Model and powder particle heating, melting, resolidification, and evaporation in plasma spraying processes, J. Heat Transfer 121 (1999) 691–699.
[12] Y.P. Wan, J.R. Fincke, S. Sampath, V. Prasad, H. Herman, Modeling and experimental observation of evaporation from oxidizing molybdenum particles entrained in a thermal plasma jet, Int. J. Heat Mass Transfer 45 (2002) 1007–1015.
[13] J.R. Fincke, W.D. Swank, D.C. Haggard, The influence of injector geometry and carrier gas flow rate on spray pattern, in: C.C. Berndt (Ed.), A United Forum for Scientific and Technological Advances, Proceedings of the National Thermal Spray Conference, USA, ASM Int., OH, USA, 1997, pp. 335–342.
[14] J.R. Fincke, W.D. Swank, D.C. Haggard, More on the influence of injector geometry and carrier gas flow rate on spray pattern and particle temperature, in: C.C. Berndt (Ed.), International Thermal Spray Conference Proceeding, ASM Inter., Materials Park, OH, USA, 2000.
[15] J. Herberlein, Electrode phenomena in plasma torches, in: P. Fauchais, J. van der Muller, J. Heberlein (Eds.), Heat

and Mass Transfer Under Plasma Conditions, Annals of the New York Academy of Sciences 891 (1999) pp. 14–27.
[16] M.I. Boulos, P. Fauchais, E. Pfender, Thermal Plasmas, Plenum Press, 1994.
[17] X. Chen, Particle heating in a thermal plasma, Pure Appl. Chem. 60 (5) (1988) 651–652.
[18] G.-X. Wang, E.F. Matthys, Modeling of nonequilibrium surface melting and resolidification for pure metals and binary alloys, Trans. ASME Heat Transfer Div. 118 (1996) 944–951.
[19] J.R. Fincke, C.H. Chang, W.D. Swank, D.C. Haggard, Entrainment and demixing in subsonic thermal plasma jets: comparison of measurements and predictions, Int. J. Heat Mass Transfer 37 (1994) 1673–1682.
[20] H.B. Xiong, L.L. Zheng, S. Sampath, J.R. Fincke, R.L. Williamson, Three-dimensional simulation of plasma spray jet, ASME Summer Heat Transfer Conference, Las Vegas, Nevada, 2003.